OPTICS

Topological engineering of terahertz light using electrically tunable exceptional point singularities

M. Said Ergoktas[1,2], Sina Soleymani[3], Nurbek Kakenov[4]†, Kaiyuan Wang[1,2], Thomas B. Smith[5]‡, Gokhan Bakan[1,2], Sinan Balci[6], Alessandro Principi[5], Kostya S. Novoselov[5], Sahin K. Ozdemir[3,7]*, Coskun Kocabas[1,2,8]*

The topological structure associated with the branch point singularity around an exceptional point (EP) can provide tools for controlling the propagation of light. Through use of graphene-based devices, we demonstrate the emergence of EPs in an electrically controlled interaction between light and a collection of organic molecules in the terahertz regime at room temperature. We show that the intensity and phase of terahertz pulses can be controlled by a gate voltage, which drives the device across the EP. Our electrically tunable system allows reconstruction of the Riemann surface associated with the complex energy landscape and provides topological control of light by tuning the loss imbalance and frequency detuning of interacting modes. Our approach provides a platform for developing topological optoelectronics and studying the manifestations of EP physics in light–matter interactions.

T he ability to understand and control light-matter interactions is fundamental to a wide range of applications in the classical and quantum domains, including but not limited to sensing, imaging, light generation, information processing, and computation. The light component in these interactions is usually in the form of electromagnetic modes confined in a resonator, whereas the matter component involves a single or a mesoscopic number of oscillators. Changing the number of oscillators coupled to a resonator is one route for achieving strong or weak light-matter coupling (1); however, this is not desirable in many practical settings as it does not lend itself to tunable and finely controllable platforms that can enable study of both weak and strong coupling regimes as well as transitions between them. The alternative is to keep the number of oscillators fixed while tuning the coupling strength and loss imbalance between the oscillators and the resonator such that the coupled oscillator-resonator system is steered between the weak and strong coupling regimes. Such non-Hermitian engineering of the system inevitably gives rise to non-Hermitian degeneracies known as exceptional points (EPs),

which coincide with the crossover point between the weak and strong coupling regimes (2–4). EPs are substantially different from the degeneracies of Hermitian systems, known as diabolic points (DPs) (5). At a DP, only the eigenvalues coalesce but the corresponding eigenstates remain orthogonal. By contrast, at an EP both the eigenvalues and the associated eigenvectors coalesce, considerably modifying the energy landscape of the system and thus resulting in reduced dimensionality and skewed topology. This, in turn, enhances the system's response to perturbations (6–9), modifies the local density of states leading to the enhancement of spontaneous emission rates (10, 11), and leads to a plethora of counterintuitive phenomena such as loss-induced lasing (12), topological energy transfer (13), enhanced chiral absorption (14), linewidth enhancement in lasers (15), unidirectional emission in ring lasers (16), and asymmetric mode switching (17).

We demonstrate the emergence of EPs in an electrically tunable platform that enables non-Hermitian engineering of the interaction of light with a collection of organic molecules in the terahertz (THz) regime. In contrast to previous demonstrations in optical (18–20), optomechanical (13, 15, 21), electronic (22), acoustic (23), and thermal systems (24)—where EPs emerge in a parameter space constructed from measurements of samples with different geometrical parameters—we observe EPs in a single fully electrically tunable device. This electrical control allows us to finely tune the losses as well as detune the system to construct voltage-controlled parameter space.

Our platform is a graphene-based tunable terahertz resonator (25), with the gate electrode forming a bottom reflective mirror and the graphene layer placed a distance away from it forming a tunable top mirror (Fig. 1A). A nonvolatile ionic liquid electrolyte layer is placed between the mirrors to achieve re-

versible gating of graphene by an applied voltage V_1 (i.e., effective gate voltage from the Dirac point), enabling an electrically tunable reflectivity and hence resonator loss. The gate electrode (a 100-nm gold film evaporated on a 50-μm-thick Kapton film) is placed on a piezo stage driven by an applied voltage V_2, forming a moveable mirror that can be used to vary the cavity length and hence tune the resonance frequency. Details regarding device fabrication are provided in (26). α-lactose crystals that support collective intermolecular vibrations at $\omega_{vib} = 0.53$ THz with a very narrow linewidth of $\gamma_{vib} = 0.023$ THz are embedded in the resonator to allow for study of the emergence of EPs in light-matter interactions (i.e., coupling between the resonator field and the α-lactose crystals) in the THz regime. α-lactose was chosen over other materials, as its smaller damping rate makes it possible to achieve strong coupling at room temperature with our graphene THz resonator.

The dynamics of this coupled system, in which an ensemble of N identical molecular vibrations of frequency ω_{vib} are coupled to a resonator mode of frequency ω_c with the same coupling strength g, are given by the complex eigenfrequencies $\omega_{\pm} = (\Delta + 2\omega_{vib})/2 - i(\Gamma + 2\gamma_{vib})/4 \pm \Omega/4$. The nonorthogonal eigenmodes are $|\psi_{\pm}\rangle \propto \begin{pmatrix} \omega_{\pm} \\ \sqrt{N}g \end{pmatrix}$. Here, $\Delta = \omega_c - \omega_{vib}$ is the frequency detuning and $\Gamma = \gamma_c - \gamma_{vib}$ represents the loss imbalance between the molecular oscillators and the resonator, whereas γ_c and γ_{vib} are the decay rates of the resonator and molecular vibrations, respectively. Finally, $\Omega = \sqrt{16Ng^2 + (2\Delta + i\Gamma)^2}$ denotes the effective coupling strength between two systems. Analysis of this expression reveals that for $\Delta = 0$ (i.e., when the field is resonant with molecular vibrations) and $\sqrt{N}g > \Gamma/4$ (i.e., strong coupling regime), the complex eigenfrequencies exhibit splitting in their real parts whereas their imaginary parts remain coalesced. On the other hand, for $\sqrt{N}g < \Gamma/4$ (i.e., weak coupling regime) they exhibit splitting in their imaginary parts whereas the real parts coalesce, implying the modification of the decay rates of the eigenstates. For $\sqrt{N}g = \pm\Gamma/4$, the complex eigenfrequencies coalesce both in their real and imaginary parts, i.e., $\omega_{\pm} = \omega_{EP} = (\omega_c + \omega_{vib})/2 - i(\gamma_c + \gamma_{vib})/4$, and in their associated eigenmodes, i.e., $|\psi_{\pm}\rangle = |\psi_{EP}\rangle \propto \begin{pmatrix} \omega_{EP} \\ \Gamma_{EP} \end{pmatrix}$ with $\Gamma_{EP} = \pm 4\sqrt{N}g$, implying the emergence of two EPs.
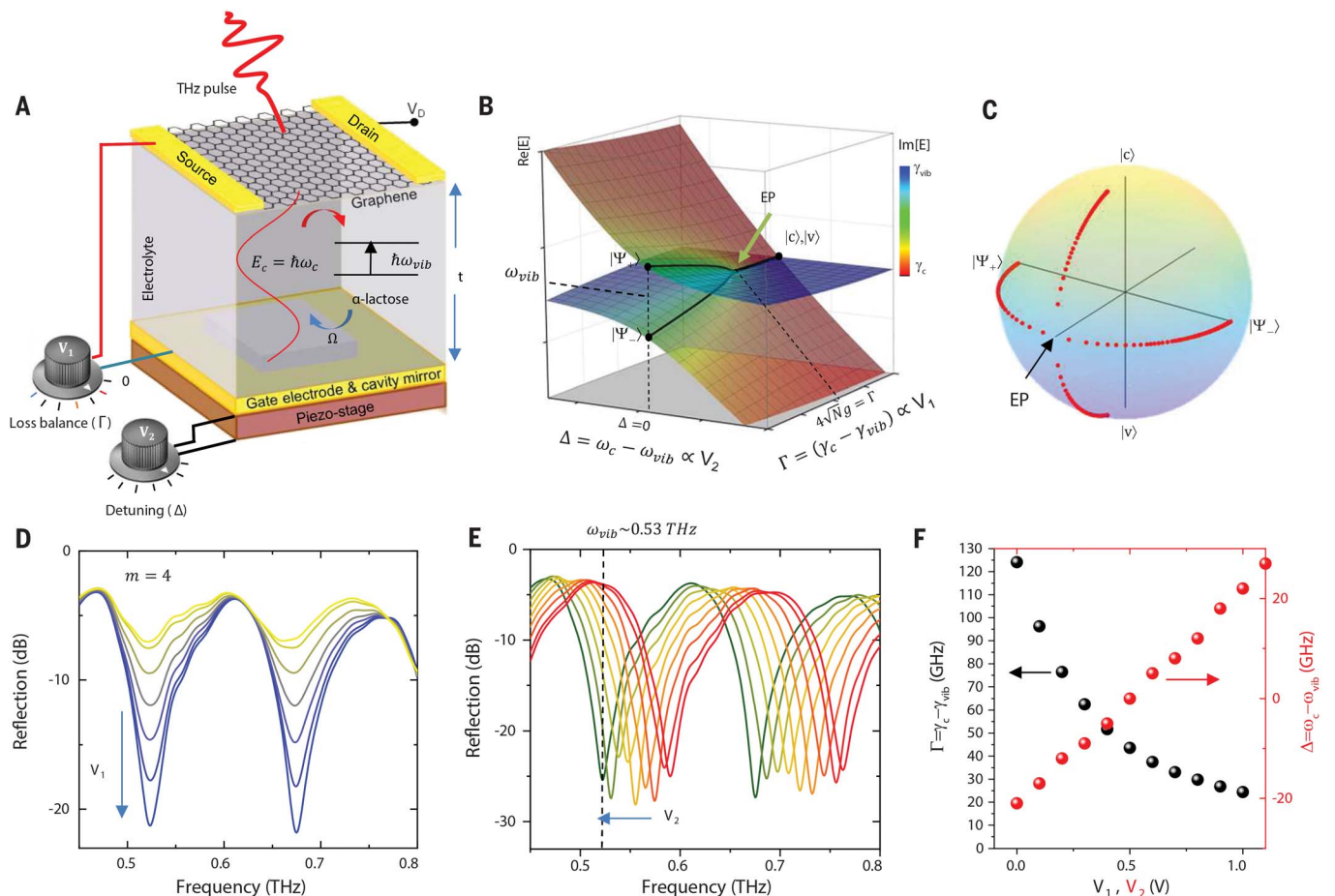
In our system (Fig. 1A), the knobs V_1 and V_2 are used to finely tune Γ and Δ, respectively, and allow us to observe the transition between the strong and weak coupling regimes through the EP. Plotting the complex energy landscape (i.e., real and imaginary parts of the complex eigenfrequencies $\omega_{\pm}$) as V_1 and V_2 are varied yields two intersecting Riemann sheets wrapped

Fig. 1. Electrically tunable EP device. (**A**) Schematic of the electrolyte-gated graphene transistor embedded with lactose microcrystals. The tunable coupling between the resonator mode $E_c = \omega_c + i\gamma_c$ and the intermolecular vibrations of lactose crystals $E_{vib} = \omega_{vib} + i\gamma_{vib}$ forms an electrically tunable two-parameter framework to realize EP devices. The gate voltage V_1 controls the loss imbalance Γ between the cavity and intermolecular vibrations by tuning the charge density on graphene, and V_2 controls the detuning frequency Δ by changing the cavity size. (**B**) Riemann surface obtained through numerical simulations shows the complex energy eigenvalues of the device plotted on the two-parameter voltage space defined by V_1 and V_2. EP emerges when the coupling strengths compensates the loss imbalance $\sqrt{N}g = \pm\Gamma/4$, when the cavity field and the intermolecular vibrations are on resonant $\Delta = \omega_c - \omega_{vib} = 0$. (**C**) Visualization of the evolution of the supermodes of the coupled system on a Bloch sphere as the gate voltage V_1 is varied (loss imbalance Γ is tuned). The azimuthal angle on the sphere indicates the relative phase, the polar angle represents the relative intensity of the uncoupled cavity (photon mode), and the collective molecular vibrations (matter mode) are represented by the eigenmodes $|c\rangle$ and $|v\rangle$, respectively. (**D** and **E**) THz reflection spectrum of the graphene cavity without lactose molecules but with the electrolyte showing the dependence of the cavity mode $|c\rangle$ on V_1 and V_2, respectively. (**F**) Voltage dependence of the loss imbalance Γ and detuning Δ of the system.

around a second-order EP right in the center where the two complex eigenfrequencies of the system coalesce (Fig. 1B). Representing the eigenstates of the system on the Bloch sphere (Fig. 1C) allows us to monitor the evolution of the state of the system during the transition from weak to strong coupling through the EP. In largely detuned or large loss imbalance cases (i.e., $\Delta \to \infty$ or $\Gamma \gg \sqrt{N}g$, that is, the limit of the uncoupled modes), the two supermodes of the system approach to the individual uncoupled electromagnetic mode (cavity photonic mode) and the matter mode (vibrational mode), which are located at the north and the south poles of the Bloch sphere, respectively. For $\Delta = 0$, varying V_1 and hence Γ gradually shifts the supermodes from the poles distributing them across the cavity and the matter (α-lactose

crystals). The supermode close to the north pole mostly resides in the cavity (cavity-like mode) whereas the supermode close to the south pole mostly resides in the matter (matter-like mode). With further tuning of Γ, the cavity-like mode $|c\rangle$ moves downward from the north pole, whereas the matter-like mode $|v\rangle$ moves upward from the south pole toward the equator. These modes then coalesce to the single mode $|\psi_{EP}\rangle$ on the equator at the critical value $\Gamma_{EP} = \pm 4\sqrt{N}g$, where dual EPs emerge.

We first confirm the effects of tuning knobs V_1 and V_2 (Fig. 1A) on the reflectivity of the empty THz resonator. As the voltage V_1—which controls the cavity loss (and hence the loss imbalance Γ of the couple)—is increased, the resonance frequency ω_c of the resonator remains intact, but the linewidth (proportional

to the decay rate γ_c) of the cavity resonance becomes narrower and the resonance depth increases, approaching critical coupling (Fig. 1D). The second knob V_2 (cavity voltage) controls the length of the resonator and its resonance frequency ω_c by moving a piezo stage (hence the gate electrode) with respect to the graphene transistor with a resolution of <6 nm. This helps finely adjust the frequency detuning Δ. It is clearly seen that as V_2 is varied, the resonance frequency ω_c of the THz resonator shifts with no considerable variation in the resonance linewidth (Fig. 1E). Because these processes do not have any effect on the vibrational frequency and decay rate of the molecules, knobs V_1 and V_2 effectively control the two-dimensional parameter space of Δ and Γ. We observed a tunability of $\sim\pm25$ GHz in Δ and

100 GHz in Γ when V_1 and V_2 were increased from 0 to 1 V (Fig. 1F). As a result, the knobs enable non-Hermitian engineering of the light-matter interaction between the THz resonator field and the collective intermolecular vibrations and allow us to map the complex energy landscape of the hybrid system.

Next, time-domain THz spectroscopy demonstrates the tunable transition between the weak and strong coupling regimes through an EP. We first tuned V_2 to have $\Delta = 0$ and then varied the gate voltage V_1, which controls the loss imbalance of the couples. As V_1 is increased, the formation of the characteristic polariton branching around ω_{vib} is clearly observed in the reflectivity map of the device (Fig. 2A). This branching takes place at two symmetric EPs $V_{EP} = \pm 0.2V$ as a result of the ambipolar electrical conduction of graphene. A cross section of this reflectivity map around one of these EPs reveals the transition from a split
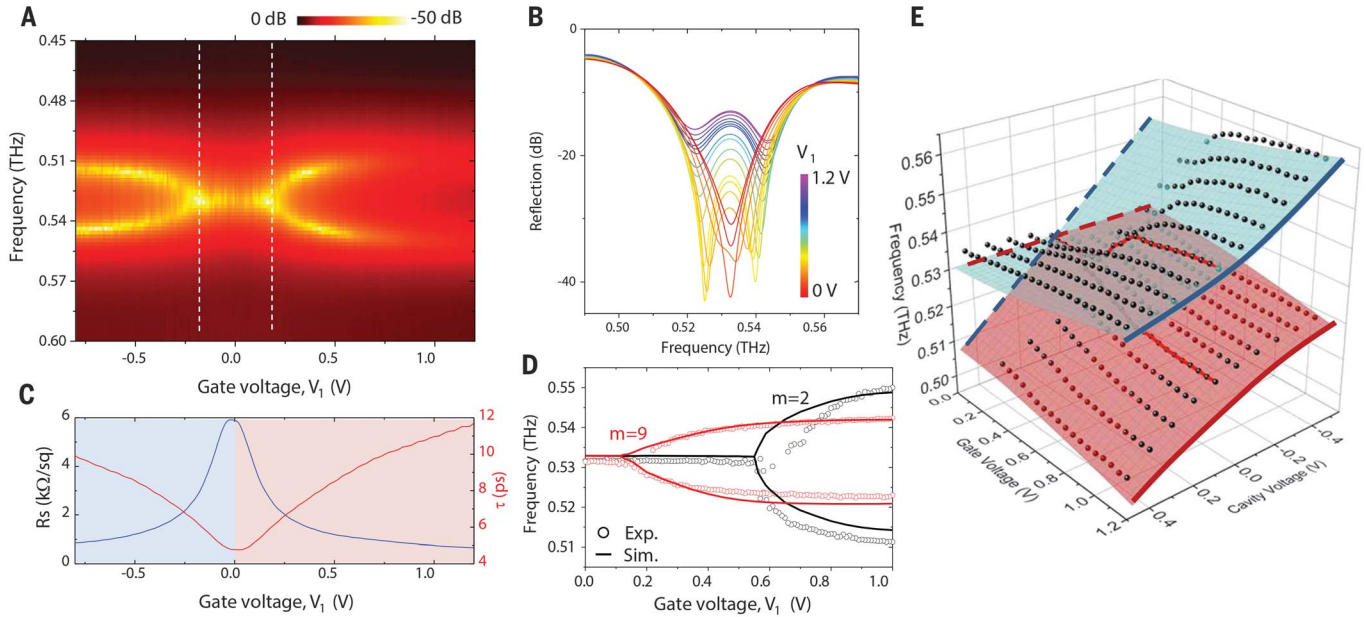
Fig. 2. Spectroscopic characterization of the EP device. (**A** and **B**) Reflectivity map and spectra of the device showing the transition from the weak (coalesced modes) to the strong coupling (split modes) regimes through an EP as V_1 is varied (Γ is tuned) at constant V_2, satisfying $\Delta = 0$. Because of the ambipolar conduction of graphene, the device goes through two EPs at $V_{EP1} = -0.2V$ (electron doping) and $V_{EP2} = 0.2V$ (hole doping). (**C**) Sheet resistance of graphene and cavity decay time plotted against the gate voltage. Increasing the gate voltage enhances the THz reflectivity of the graphene mirror, leading to a longer cavity decay time. (**D**) Position of the EP and the amount of splitting vary with the mode number m. EPs emerge at smaller gate voltages for higher m. (**E**) Riemann surfaces obtained experimentally (black dotted) and through calculations (blue and red sheets) showing the real part of complex eigenvalues of the device in the voltage-controlled parameter space.
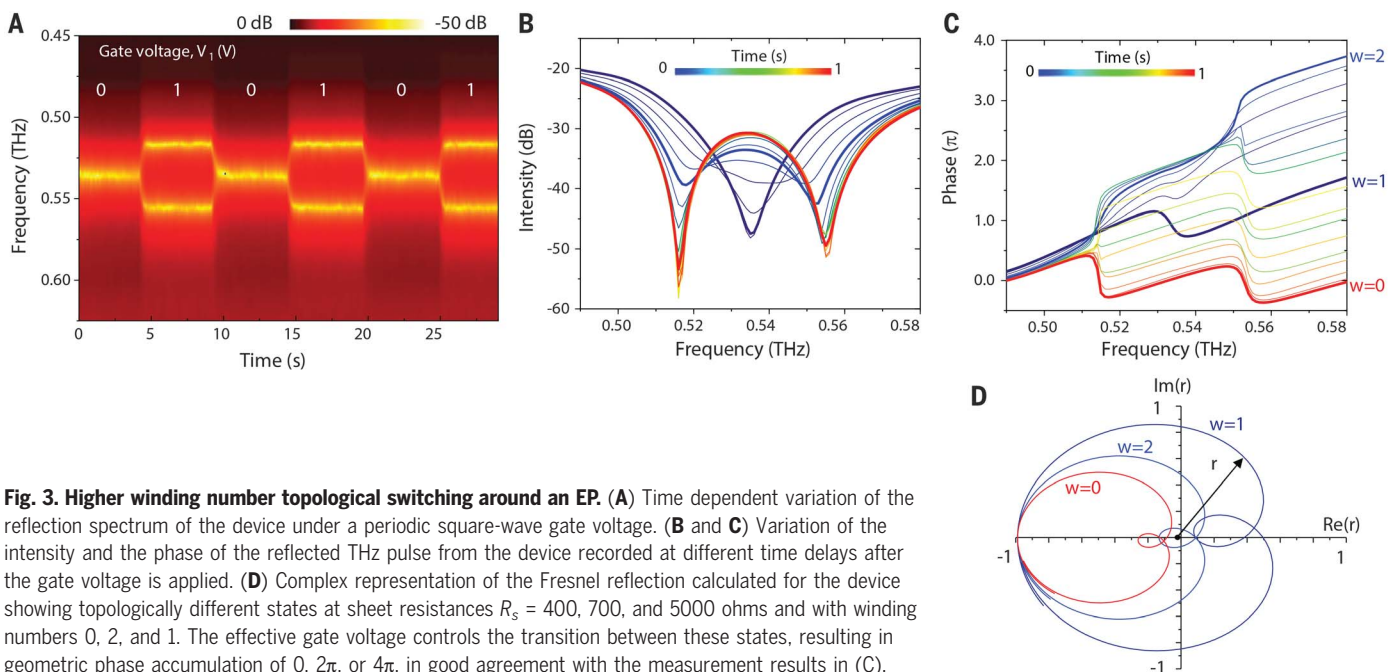
Fig. 3. Higher winding number topological switching around an EP. (**A**) Time dependent variation of the reflection spectrum of the device under a periodic square-wave gate voltage. (**B** and **C**) Variation of the intensity and the phase of the reflected THz pulse from the device recorded at different time delays after the gate voltage is applied. (**D**) Complex representation of the Fresnel reflection calculated for the device showing topologically different states at sheet resistances $R_s = 400$, 700, and 5000 ohms and with winding numbers 0, 2, and 1. The effective gate voltage controls the transition between these states, resulting in geometric phase accumulation of 0, 2π, or 4π, in good agreement with the measurement results in (C).

mode spectrum (i.e., strong coupling regime) to a coalesced mode spectrum (i.e., weak coupling regime) through the EP (Fig. 2B). The transition between these two regimes as V_1 is varied can be attributed to the variation of the optical conductivity of graphene and the corresponding cavity decay time (Fig. 2C). This dependence on V_1 clarifies our ability to control loss imbalance between the couples through the control of the resonator losses.

Experiments with different cavity modes (from $m = 2$ to 9, adjusted by tuning the cavity size) satisfying $\Delta = 0$ reveal that the transition from the split modes to coalesced modes occurs at different V_1 voltages for different cavity modes (Fig. 2D): The higher the mode number m, the smaller the required gate voltage V_1 to arrive at the EP. This behavior may be attributed to (i) the larger mode volume (and hence lower field strength) and thus the reduced effective coupling strength at higher m or (ii) the smaller γ_c of higher-order modes and thus smaller initial loss imbalance between the couples. As a result, the amount of additional loss imbalance required to satisfy the EP condition $\sqrt{N}g = \Gamma/4$ is smaller for higher-order cavity modes, implying that modes with higher m require smaller gate voltage V_1 to reach EP. Because the EP is a singularity point in the two-parameter space, we have finely tuned Γ and Δ through the knobs V_1 and V_2 for a fixed mode m and reconstructed the Riemann surface associated with the complex energy landscape of the system (Fig. 2E). The topology of two intersecting Riemann sheets centered around an EP is clearly seen (Figs. 1B and 2E). From the experimentally determined maximum frequency splitting values, we estimate the number of molecules contributing to the process as ~10^{18} for all cavity modes (26).

Next, we investigate the electrical control of EP and its effect on the intensity and the phase of the reflected THz light. For this purpose, we prepare the system at $\Delta = 0$ and dynamically modulate the loss imbalance Γ by applying a periodic square-wave gate voltage V_1. The time-dependent reflection spectra clearly show periodic splitting and coalescence of the modes (Fig. 3A). The system gradually transits from the coalesced modes ~0.535 THz to split modes with a splitting of ~40 GHz in 0.2 s after the gate voltage is set to the "ON" state. We recorded the intensity (Fig. 3B) and the phase (Fig. 3C) of the reflected THz pulse from the device at different time delays after the ON signal is applied. We must point out that the measured phase depends on the reference plane; however, the phase difference is uniquely defined. We observe a phase accumulation of 0, 2π, and 4π across the free spectral range of the resonator during the transition through the EP. This geometrical (i.e., Berry) phase is the result of the topology of the Fresnel reflectivity $r(\omega)$. Here the topological invariant is the winding

number $n = \frac{1}{2\pi i}\oint \frac{dr}{r}$ of the complex Fresnel reflectivity around the perfect absorption singularity ($r = 0$; critical coupling) in which the reflection phase is undefined. Calculated reflection (Fig. 3D) for our device at three different sheet resistances reveals three topologically different reflectivities identified by winding numbers $n = 0$, 1, and 2 and the associated Berry phases of 0, 2π, or 4π, respectively, agreeing with the phases measured in the experiments (Fig. 3C). These results provide the first direct evidence for the electrically switchable reflection topology.

One of the most notable features of an EP is the exchange of the eigenstate when it is adiabatically encircled. This contrasts with encircling a DP in Hermitian systems where the eigenstate acquires a geometric phase and no state flip takes place. Although one loop around the EP flips the eigenstate, only the second loop returns the system to its initial state apart from a Berry phase π. State flip when encircling EPs has been experimentally demonstrated with static measurements from a series of samples including microwave cavities (27), optical resonators (28), exciton-polariton systems (19, 29), and acoustic systems (23). Here, we probe our system when it is steered on cyclic paths encircling an EP by tuning Γ and Δ with the knobs V_1 and V_2. This is possible in our system because the two finely controlled knobs are independent. By varying V_1 and V_2 in steps of 25 mV such that an EP is encircled in the clockwise or counterclockwise directions, we monitor how the final state of the system is affected by the encircling process. In order to do this, we defined a loop by the points $\{\Delta_{max}, \Gamma_{min}\}$, $\{\Delta_{max}, \Gamma_{max}\}$, $\{\Delta_{min}, \Gamma_{max}\}$, $\{\Delta_{min}, \Gamma_{min}\}$ returning back to $\{\Delta_{max}, \Gamma_{min}\}$ after ~20 s. Similarly, in the parameter space of V_1 and V_2, the loop is defined by the corresponding voltage points as $\{V_{2max}, V_{1min}\}$, $\{V_{2max}, V_{1max}\}$, $\{V_{2min}, V_{1max}\}$, $\{V_{2min}, V_{1min}\}$ returning back to $\{V_{2max}, V_{1min}\}$. When we choose a control loop that does not enclose the EP, the system returns to the same state at the end of the loop (Fig. 4A), regardless of whether the loop is clockwise or counterclockwise. By contrast, when the loop encircles the EP, we observe that a trajectory starting on one of the Riemann sheets ends on the other sheet (Fig. 4B), resulting in eigenstate exchange (state flip): $|\psi_+\rangle \rightarrow |\psi_-\rangle$ and $|\psi_-\rangle \rightarrow |\psi_+\rangle$. To gain more insight on these dynamics, we illustrate the evolution of the
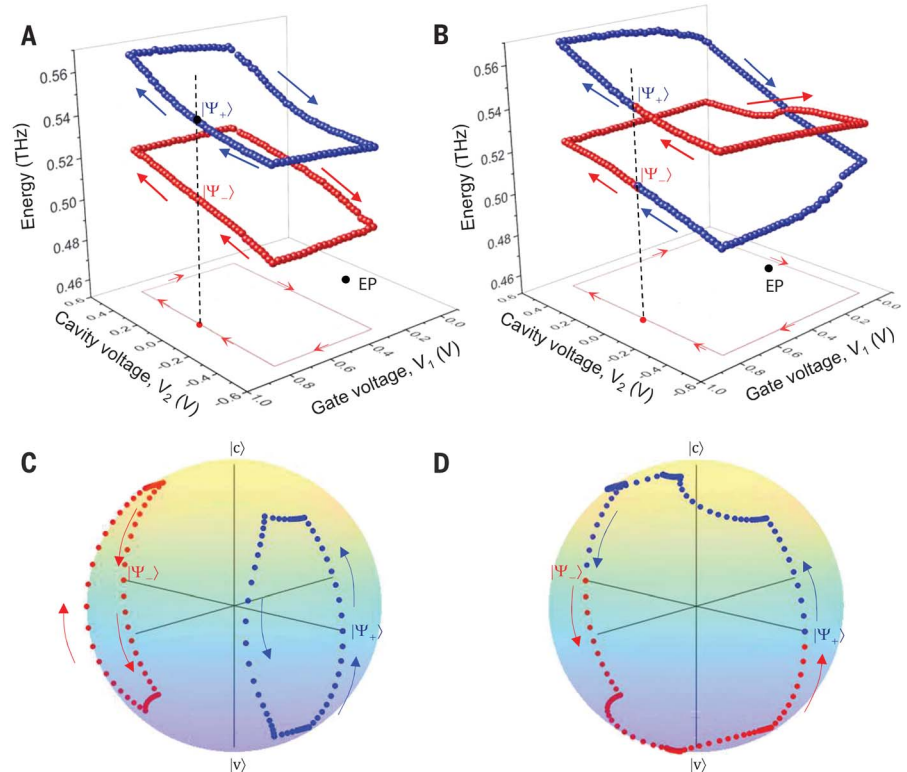
Fig. 4. Voltage-controlled encircling of EP. (**A** and **B**) Evolution of the energy of the coupled system along the trajectories traced by varying the voltages V_1 and V_2 in small steps. (A) A trajectory starting on one of the Riemann sheets stays on the same sheet if it does not encircle the EP. (B) A trajectory starting on one of the Riemann sheets ends on the other sheet (state exchange) if it encircles the EP. (**C** and **D**) Evolution of eigenstates of the system on the Bloch sphere for the trajectories shown in (A) and (B), respectively.

eigenstates of the system on Bloch spheres for closed loops that do (Fig. 4D) and do not (Fig. 4C) encircle the EP. When the system is initially in the state $|\psi_+\rangle = (|c\rangle + |v\rangle)/\sqrt{2}$, which is the equal to the superposition of the cavity $|c\rangle$ and vibrational $|v\rangle$ modes, the final state after a closed loop encircling the EP becomes $|\psi_-\rangle = (|c\rangle - |v\rangle)/\sqrt{2}$, which is orthogonal to the initial state $|\psi_+\rangle$. A second loop around the EP brings the system back to its initial state $|\psi_+\rangle$ apart from a geometrical phase. As seen in the Bloch sphere (Fig. 4D), these two loops around the EP cut the Bloch sphere directly in half and correspond to a solid angle of 2π, which in turn implies that the acquired geometrical phase is π (i.e., the geometrical phase is the half of the solid angle enclosed by the curve connecting the initial and final states).

We have demonstrated a non-Hermitian optical device to study EP in the collective interaction of vibrational modes of organic molecules with a THz field. Through use of fully electrically tunable independent knobs, we can steer the system through an EP that enables electrical control on reflection topology. Our results provide a platform for the topological control of light-matter interactions around an EP, with potential applications ranging from topological optoelectronic devices to topological control of physical and chemical processes.

REFERENCES AND NOTES

1. P. A. Thomas, W. J. Tan, H. A. Fernandez, W. L. Barnes, *Nano Lett.* **20**, 6412–6419 (2020).
2. M. A. Miri, A. Alù, *Science* **363**, eaar7709 (2019).
3. S. K. Özdemir, S. Rotter, F. Nori, L. Yang, *Nat. Mater.* **18**, 783–798 (2019).
4. R. El-Ganainy et al., *Nat. Phys.* **14**, 11–19 (2018).
5. C. M. Bender, S. Boettcher, *Phys. Rev. Lett.* **80**, 5243–5246 (1998).
6. W. Chen, Ş. K. Özdemir, G. Zhao, J. Wiersig, L. Yang, *Nature* **548**, 192–196 (2017).
7. H. Hodaei et al., *Nature* **548**, 187–191 (2017).
8. Y. H. Lai, Y. K. Lu, M. G. Suh, Z. Yuan, K. Vahala, *Nature* **576**, 65–69 (2019).
9. M. P. Hokmabadi, A. Schumer, D. N. Christodoulides, M. Khajavikhan, *Nature* **576**, 70–74 (2019).
10. A. Pick et al., *Opt. Express* **25**, 12325–12348 (2017).
11. Q. Zhong, A. Hashemi, Ş. K. Özdemir, R. El-Ganainy, *Phys. Rev. Res.* **3**, 013220 (2021).
12. B. Peng et al., *Science* **346**, 328–332 (2014).
13. H. Xu, D. Mason, L. Jiang, J. G. E. Harris, *Nature* **537**, 80–83 (2016).
14. S. Soleymani et al., *Nat. Commun.* **13**, 599 (2022).
15. J. Zhang et al., *Nat. Photonics* **12**, 479–484 (2018).
16. B. Peng et al., *Proc. Natl. Acad. Sci. U.S.A.* **113**, 6845–6850 (2016).
17. J. Doppler et al., *Nature* **537**, 76–79 (2016).
18. J. B. Khurgin, *Optica* **7**, 1015 (2020).
19. W. Gao, X. Li, M. Bamba, J. Kono, *Nat. Photonics* **12**, 362–367 (2018).
20. B. Peng et al., *Nat. Phys.* **10**, 394–398 (2014).
21. H. Jing et al., *Phys. Rev. Lett.* **113**, 053604 (2014).
22. M. Geiser, G. Scalari, F. Castellano, M. Beck, J. Faist, *Appl. Phys. Lett.* **101**, 141118 (2012).
23. K. Ding, G. Ma, M. Xiao, Z. Q. Zhang, C. T. Chan, *Phys. Rev. X* **6**, 021007 (2016).
24. Y. Li et al., *Science* **364**, 170–173 (2019).
25. N. Kakenov, M. S. Ergoktas, O. Balci, C. Kocabas, *2D Materials* **5**, 035018 (2018).
26. Materials and methods are available as supplementary materials.
27. C. Dembowski et al., *Phys. Rev. Lett.* **86**, 787–790 (2001).
28. S. B. Lee et al., *Phys. Rev. Lett.* **103**, 134101 (2009).
29. T. Gao et al., *Nature* **526**, 554–558 (2015).
30. M. S. Ergoktas et al., Topological engineering of terahertz light using electrically tunable exceptional point singularities, version 1, Zenodo (2022); https://doi.org/10.5281/zenodo.6105427.

SUPPLEMENTARY MATERIALS

science.org/doi/10.1126/science.abn6528
Materials and Methods
Supplementary Text
Figs. S1 to S13
References (31–35)

10 December 2021; accepted 10 March 2022
10.1126/science.abn6528